# the plant journal



The Plant Journal (2023) 113, 887-903

doi: 10.1111/tpj.16101

# Image-based assessment of plant disease progression identifies new genetic loci for resistance to *Ralstonia* solanacearum in tomato

Valérian Méline<sup>1</sup>, Denise L. Caldwell<sup>1</sup>, Bong-Suk Kim<sup>1</sup>, Rajdeep S. Khangura<sup>2</sup>, Sriram Baireddy<sup>3</sup>, Changye Yang<sup>3</sup>, Erin E. Sparks<sup>4</sup>, Brian Dilkes<sup>2</sup>, Edward J. Delp<sup>3</sup> and Anjali S. Iyer-Pascuzzi<sup>1,\*</sup>

Received 21 July 2022; revised 12 November 2022; accepted 2 January 2023; published online 10 January 2023. \*For correspondence (e-mail asi2@purdue.edu).

#### **SUMMARY**

A major challenge in global crop production is mitigating yield loss due to plant diseases. One of the best strategies to control these losses is through breeding for disease resistance. One barrier to the identification of resistance genes is the quantification of disease severity, which is typically based on the determination of a subjective score by a human observer. We hypothesized that image-based, non-destructive measurements of plant morphology over an extended period after pathogen infection would capture subtle quantitative differences between genotypes, and thus enable identification of new disease resistance loci. To test this, we inoculated a genetically diverse biparental mapping population of tomato (*Solanum lycopersicum*) with *Ralstonia solanacearum*, a soilborne pathogen that causes bacterial wilt disease. We acquired over 40 000 timeseries images of disease progression in this population, and developed an image analysis pipeline providing a suite of 10 traits to quantify bacterial wilt disease based on plant shape and size. Quantitative trait locus (QTL) analyses using image-based phenotyping for single and multi-traits identified QTLs that were both unique and shared compared with those identified by human assessment of wilting, and could detect QTLs earlier than human assessment. Expanding the phenotypic space of disease with image-based, non-destructive phenotyping both allowed earlier detection and identified new genetic components of resistance.

Keywords: digital phenotyping, quantitative trait loci, Ralstonia solanacearum, Solanum lycopersicum, bacterial wilt, tomato.

**Linked article**: This paper is the subject of a Research Highlight article. To view this Research Highlight article visit https://doi.org/10.1111/tpj.16138.

#### INTRODUCTION

Plant diseases are a significant global constraint to crop production. Developing disease-resistant crops requires identification of genes and alleles which allow crops to resist the pathogenic microbes that cause disease. Identification of disease resistance loci requires phenotyping of genetically diverse populations of plants that differ in their response to pathogen infection. Phenotyping plant diseases is challenging because diseases cause complex, quantitative phenotypes that can occur across spatiotemporal scales throughout the development of a plant – e.g.,

on parts of leaves, entire leaves, or the whole plant. Disease phenotypes vary over time and are modulated by environmental conditions, plant age, and pathogen virulence. Disease symptoms such as wilting or necrotic spots are frequently given a visual score, but such phenotypic assessments are subjective as they can differ by individual or scoring scale, leading to variable estimates of disease severity.

The challenging nature of visual disease assessment has led to the use of imaging techniques that deploy RGB, hyperspectral, chlorophyll fluorescence, and thermal

<sup>&</sup>lt;sup>1</sup>Department of Botany and Plant Pathology and Center for Plant Biology, Purdue University, 915 W. State Street, West Lafayette, Indiana, USA,

<sup>&</sup>lt;sup>2</sup>Department of Biochemistry and Center for Plant Biology, Purdue University, West Lafayette, Indiana, 47907, USA,

<sup>&</sup>lt;sup>3</sup>Video and Image Processing Laboratory (VIPER), School of Electrical and Computer Engineering, Purdue University, West Lafayette, Indiana, USA, and

<sup>&</sup>lt;sup>4</sup>Department of Plant and Soil Sciences and the Delaware Biotechnology Institute, University of Delaware, Newark, Delaware, USA

cameras to assess disease severity (Bock et al., 2010; Colwell, 1956; Jackson, 1986; Simko et al., 2017). Compared to assessment by the human eye, image-based phenotyping is more reproducible and can capture even subtle variations in disease symptoms, which enables sensitive detection of resistance loci (Bock et al., 2008, 2010; Shakoor et al., 2017; Simko et al., 2017; Stewart et al., 2016; Stewart & McDonald, 2014). Many studies have used or developed tools to assess plant symptoms using different types of sensors (Lowe et al., 2017; Mahlein, 2016; Mahlein et al., 2017, 2019; Mir et al., 2019; Mochida et al., 2019; Pérez-Bueno et al., 2019; Pineda et al., 2021; Shakoor et al., 2017; Simko et al., 2017). However, only a few studies have used these image- or sensor-based phenotypes to carry out quantitative trait locus (QTL) or genome-wide association (GWA) analyses for responses to plant pathogens, and all have used destructive methods (Barbacci et al., 2020; Corwin et al., 2016; Fordyce et al., 2018; Yates et al., 2019). It has remained challenging to use imagebased, non-destructive phenotyping for disease resistance across large populations, because of both technical limitations like the expertise, time, and expense to develop phenotyping platforms and biological factors which limit the utility of any simple parameter (such as plant size) for accurately reporting disease severity within diverse populations and across time. One benefit of image-based phenotyping is that it can be used to capture both singular geometric traits and compound higher-order traits. For example, image-based phenotyping can capture plant height, width, and color as single traits. However, these are not independently controlled traits from a plant perspective, and the artificial separation of these traits into single values may limit the resolution of our genetic detection approaches. These single trait values can be combined into one or more holistic multi-traits that captures a more comprehensive view of the phenotype, allowing for the detection of new loci associated with the response.

The Ralstonia solanacearum species complex (RSSC) is the causal agent of bacterial wilt disease and has been ranked as one of the top 10 most destructive plant bacterial pathogens of all time (Mansfield et al., 2012). Due to high levels of genetic diversity within the RSSC, the pathogen is called a species complex and was recently subdivided into three related species (Prior et al., 2016; Safni et al., 2014; Sharma et al., 2022). Strains in the RSSC have different host ranges, virulence proteins, metabolic requirements, and centers of origin (García et al., 2019; Prior et al., 2016). Here we use 'Ralstonia' to refer to the entire species complex. Ralstonia infects root systems of both resistant and susceptible plants (Caldwell et al., 2017; French et al., 2018; Planas-Marquès et al., 2020). After entering the root, Ralstonia multiplies in the xylem and subsequently moves into the shoot vasculature. Exopolysaccharide produced by bacteria acts like a plug in the xylem (Ingel et al., 2021),

preventing water flow to the shoot and leading to wilting in susceptible plants, whereas resistant plants restrict bacterial growth within the xylem and do not wilt (Caldwell et al., 2017; Planas-Marquès et al., 2020). Wilting is therefore used to estimate the level of susceptibility of plants to Ralstonia infection (Genin, 2010; Genin & Denny, 2011). This bacterium is a major production constraint in solanaceous crops globally, including the United States, with yield losses in tomatoes (Solanum lycopersicum) reported to be over 70% (Elphinstone et al., 2005; Yuliar et al., 2015). Resistance to Ralstonia is quantitative in nature (Kim et al., 2016; Scott et al., 2005; Yuliar et al., 2015), but the QTLs underlying resistance to US strains of Ralstonia are largely unknown. QTLs for resistance to non-US Ralstonia strains have been mapped (Carmeille et al., 2006; Danesh et al., 1994; Mangin et al., 1999; Shin et al., 2020; Thoquet, Olivier, Sperisen, Rogowsky, Laterrot, et al., 1996; Thoquet, Olivier, Sperisen, Rogowsky, Prior, et al., 1996; Wang et al., 2000, 2013), but functional characterization of the candidate genes underlying the QTLs and the host determinants necessary for resistance remain unknown.

The limited characterization of QTLs for Ralstonia resistance can be attributed in part to the difficulty in accurately scoring plant wilting. Wilting is traditionally measured on a subjective scale, in which researchers estimate the percentage of wilted leaves (Schandry, 2017). While it is straightforward to assess the extreme ends of the spectrum, rating plants with mid-range scores is particularly difficult. This is due to the subjective nature of visually determining when a leaf has lost sufficient turgor to qualify as wilted. Reliable and reproducible disease phenotyping is critical for identifying QTLs for resistance to Ralstonia and the development of resistant varieties.

Here, we report an image-based, rapid, nondestructive phenotyping pipeline that was used to identify novel loci in tomato that impart resistance to R. solanacearum strain K60 (hereafter R. solanacearum). We developed a rapid, semi-automated imaging and trait analysis pipeline to quantify bacterial wilt disease and applied it in a recombinant inbred line (RIL) population derived from R. solanacearum-resistant and susceptible tomato genotypes. We found both unique and shared QTLs between our image-based traits and a subjective plant wilting score. Employing a dimension reduction approach to develop compound multi-traits, we were able to detect additional QTLs and further enhance our analysis. QTLs for wilting were detected by image-based phenotyping before the onset of visual symptoms, demonstrating that welldesigned image-based phenotyping captures the disease phenotype at early stages of infection. These results demonstrate that image-based, non-destructive phenotyping can shed light on new aspects of disease and improve our ability to identify loci that can be used to breed disease-resistant crops.

# **RESULTS**

# Development of an aboveground imaging and semiautomated image analysis pipeline

We constructed a simple, low-cost imaging system that allowed us to semi-automate aboveground disease phenotyping. Each plant was placed on a commercially available turntable, and plants were imaged with a Canon DSLR camera (Figure S1; details in Methods section). The camera was connected with a PhotoCapture 360 turntable (Ortery technologies, Irvine, CA, USA), which allowed us to automatically capture images every 45° (eight images per plant). Using this system, we were able to nondestructively image each plant in less than 2 min, with minimal manual labor. Each image included a fiducial marker for post-image color correction.

Non-destructive imaging permitted repeated phenotyping. Plants were imaged the day before inoculation with R. solanacearum and at 3, 4, 5, and 6 days post-inoculation (dpi). We imaged five replicate plants of each RIL as well as the parental lines. Using this system, we captured over 40 000 images for high-resolution disease phenotyping. The same set of plants were also visually scored by the same individual at all time points used for imaging and also at 8 dpi. Visual scoring was based on the percentage of wilted leaves (Figure S2). At 3 dpi, subjectively assessed wilting disease symptoms were not present in the susceptible parent West Virginia 700 (WV). By 6 dpi, however, these plants were completely wilted. The disease phenotypes in the RIL population ranged from highly susceptible to highly resistant, consistent with segregating resistance loci that impart varying degree of resistance to R. solanacearum in a quantitative manner (Figure S3).

We next developed a set of mathematical descriptors to phenotype plants for wilting over time in our images. Plant wilting is a composite phenotype, and we used 10 image-based traits (Figure 1) to quantify different aspects of wilting: convex area, convex width, convex perimeter,

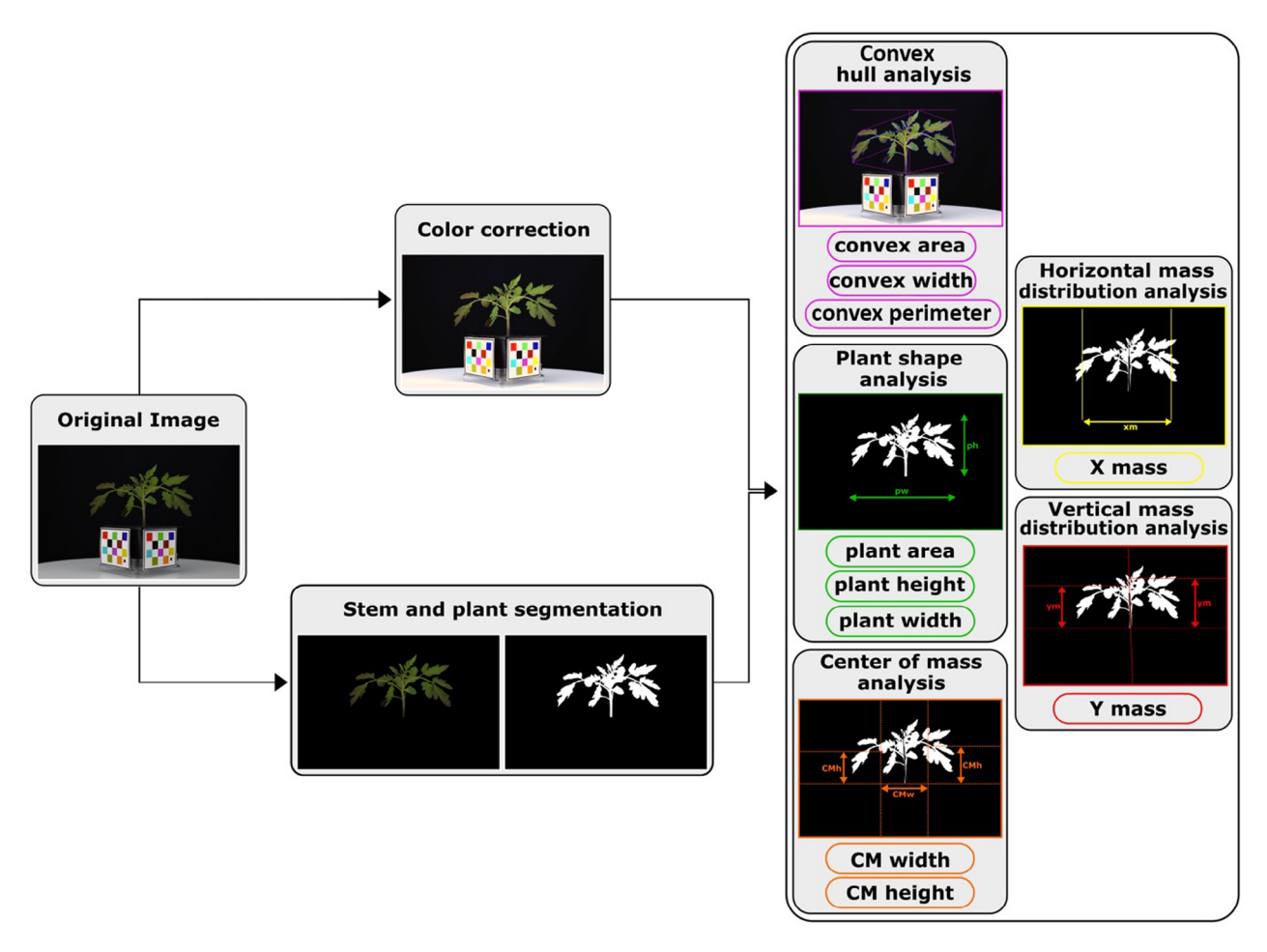


Figure 1. Diagram of the semi-automated analysis pipeline and 10 image descriptors. After the original image is captured, the image is color-corrected and segmented to identify the stem and plant. From the color-corrected image, convex area, width, and color are quantified. From the segmented image, the plant area, height, width, X mass, Y mass, CM width, and CM height are calculated. For further details, see Methods section.

plant area, plant width, plant height, X mass, Y mass, center of mass (CM) height, and CM width. Several of these, such as the area and width of the convex hull, are indices that are traditionally used to describe aboveground plant shape. Because the CM of a plant leaf changes as a plant wilts, we developed additional descriptors based on the distance of the leaf CM from the stem (CM width and CM height, X mass and Y mass). We then developed a pipeline which used the original image as input, performed color correction, and quantified each descriptor (Figure 1; Figure S4, and Methods section).

# Image-based traits differentiate resistant and susceptible plants

To validate the efficiency of the image-based descriptors to estimate wilting phenotypes, we tested whether imagebased phenotyping descriptors could differentiate resistant from susceptible inoculated plants. All 10 descriptors, particularly those based on plant width or convex hull, had significantly increased values in the resistant parent at 6 dpi compared to day -1 (Figure 2a) consistent with continued growth. In the susceptible parent, seven of 10 descriptors were significantly decreased at 6 dpi compared to day -1. The three descriptors that did not differ, plant height, Y mass, and convex perimeter, significantly increased immediately after inoculation and subsequently decreased. Although they were trending downward at 6 dpi, they were not significantly different at that time point compared to -1 dpi. The majority of RIL descriptor values ranged from those of the resistant to susceptible parents and with some transgressive segregation (Figure 2a).

# Image-based traits are correlated with wilting score

We next investigated how well our image-based traits correlated with human visual scoring. Wilting is categorized by loss of plant leaf turgor, which results in drooping leaves, and decreased plant width and height. Determining how much a plant has wilted is challenging, in part because it can be difficult to quantify how much each leaf has drooped and how much drooping of one leaf correlates with whole plant wilting. We aimed to quantify leaf drooping in image data by using CM traits. Among our image-based traits, those which were functions of the leaf CM were highly inversely correlated with visual wilting score (i.e., as a plant wilts, the CM decreases). These traits included convex width, CM width, plant width, and X mass (r < -0.86) (Figure 2b). Multiple image-based traits at earlier time points were correlated with wilting score at 6 dpi (Table S1). These traits included convex width, plant width, and X mass (all r < -0.6) at 4 dpi, and convex area, convex width, plant area, plant width, X mass, and CM width (all r < -0.7) at 5 dpi.

Several of our traits describe similar features of plant shape, such as height or width, through different

methods. These traits tended to be highly correlated with each other. For example, plant height versus Y mass use different methods to describe plant height (based on the plant mask or the CM of the stem masks; see Methods section), and were highly positively correlated with each other (r = 0.93; Figure 2b). Similarly, convex hull width, plant width, CM width, and X mass were highly correlated with one another (Figure 2b). While all describe plant width, they quantify different aspects of width. Convex hull width captures the maximum Euclidian distance between two points in the convex hull (regardless of direction), while plant width captures the distance between two points in the image along the x-axis (Figure S4). Additionally, these different measurements of width may be more or less informative at different levels of disease. For example, the CM width may be more influenced by severe rather than mild wilting symptoms. We chose to use all of these highly correlated, but subtly different traits because they may detect different aspects of the phenotype and thus different QTLs.

# Image-based traits differentiate mock from *R. solana-cearum*-inoculated plants

Using four resistant RILs, four susceptible RILs, the resistant parent Hawaii 7996 (H7996), and the susceptible parent WV, we asked whether the image-based traits could differentiate mock from inoculated plants. Values of all traits increased over time in mock-inoculated resistant and susceptible plants (Figure 3; Figure S5). In the resistant parent H7996 and all four resistant RILs, values of all image-based traits increased after R. solanacearum inoculation, although not always at the same rate as in the mock-inoculated plants. This was not surprising given that resistant H7996 tomatoes are colonized by R. solanacearum (Caldwell et al., 2017; French et al., 2018; Planas-Marquès et al., 2020), which may impede plant growth. In contrast to resistant lines, in R. solanacearum-inoculated susceptible parent WV and all four susceptible RILs the image-based trait values decreased compared to their mock-inoculated counterparts (Figure 3; Figure S5).

# Single-trait QTL mapping identifies 30 QTLs in 12 clusters across the tomato genome

The goal of this study was to identify genomic regions that provide resistance or susceptibility to *R. solanacearum*. To facilitate this analysis, we first generated a genetic map. We identified 632 high-quality single-nucleotide polymorphisms (SNPs) for linkage mapping using genotyping by sequencing (GBS) and combined these with 112 SolCap markers. These data were used to construct a linkage map using ICI mapping software (Meng et al., 2015). Our linkage map consisted of approximately 1300 cM (Figure 4) with an average marker density per chromosome that varied from 1.8 to 7.48 cM (Table S2).

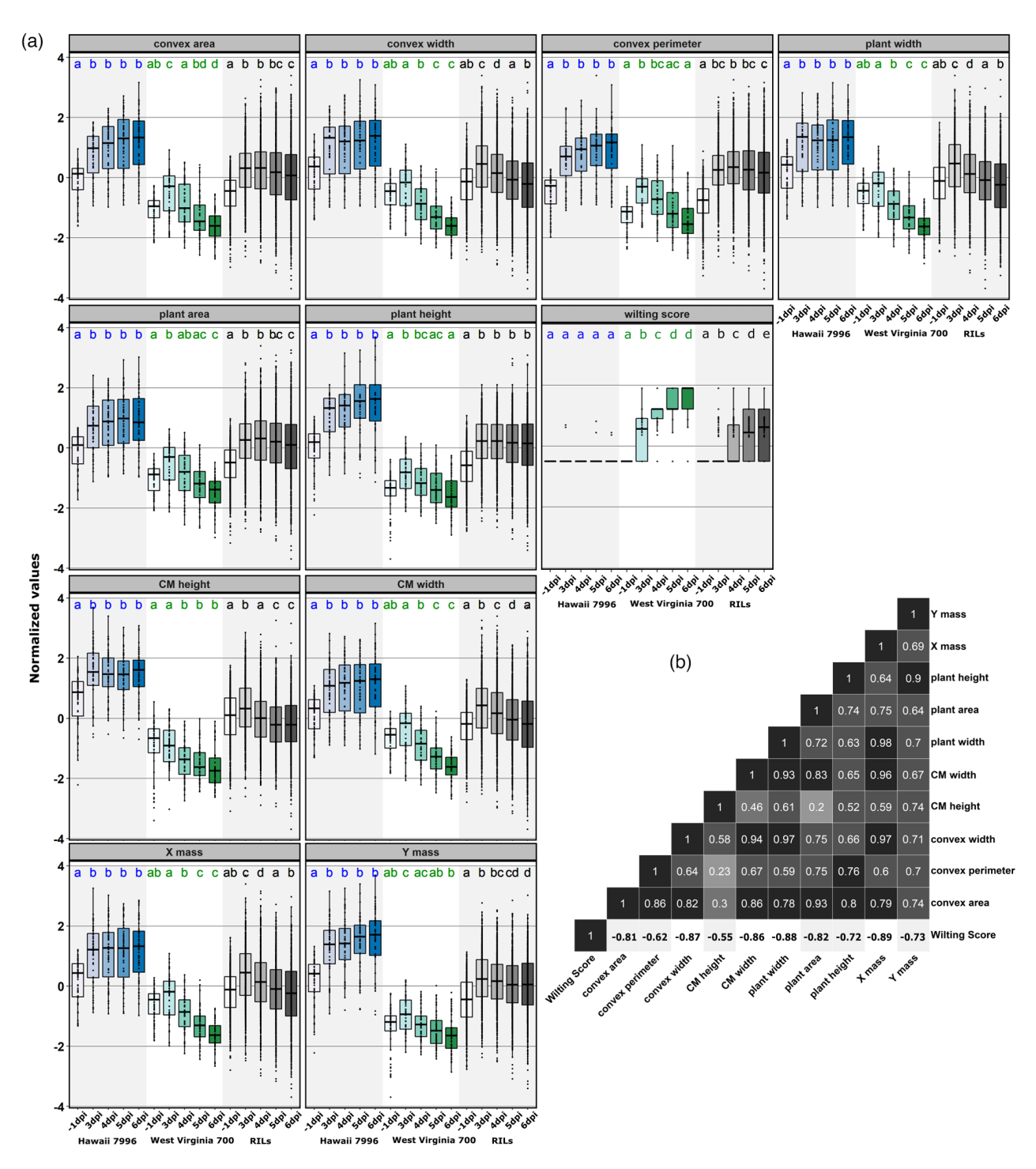


Figure 2. Trait responses to Ralstonia solanacearum and correlation among descriptors. (a) Boxplots showing the mean normalized values for image-based traits at -1, 3, 4, 5, and 6 dpi for the resistant Hawaii 7996 genotype, the susceptible West Virginia 700 genotype, and 166 individuals of the recombinant inbred line population. Letters indicate significant differences as determined with the t-test with Bonferroni correction within each genotype group.

(b) Heatmap showing the Pearson correlation values between image-based traits and the visual wilting score at 6 dpi. dpi, days post-inoculation.

Phenotypic variation between genotypes in both image-based and visual scoring was partly explained by genotypic differences. Wilting score showed a gradual increase in heritability over time with a highest value of 0.76 at 8 dpi. This is consistent with the notion that visual assessment of inherent susceptibility of a plant is more

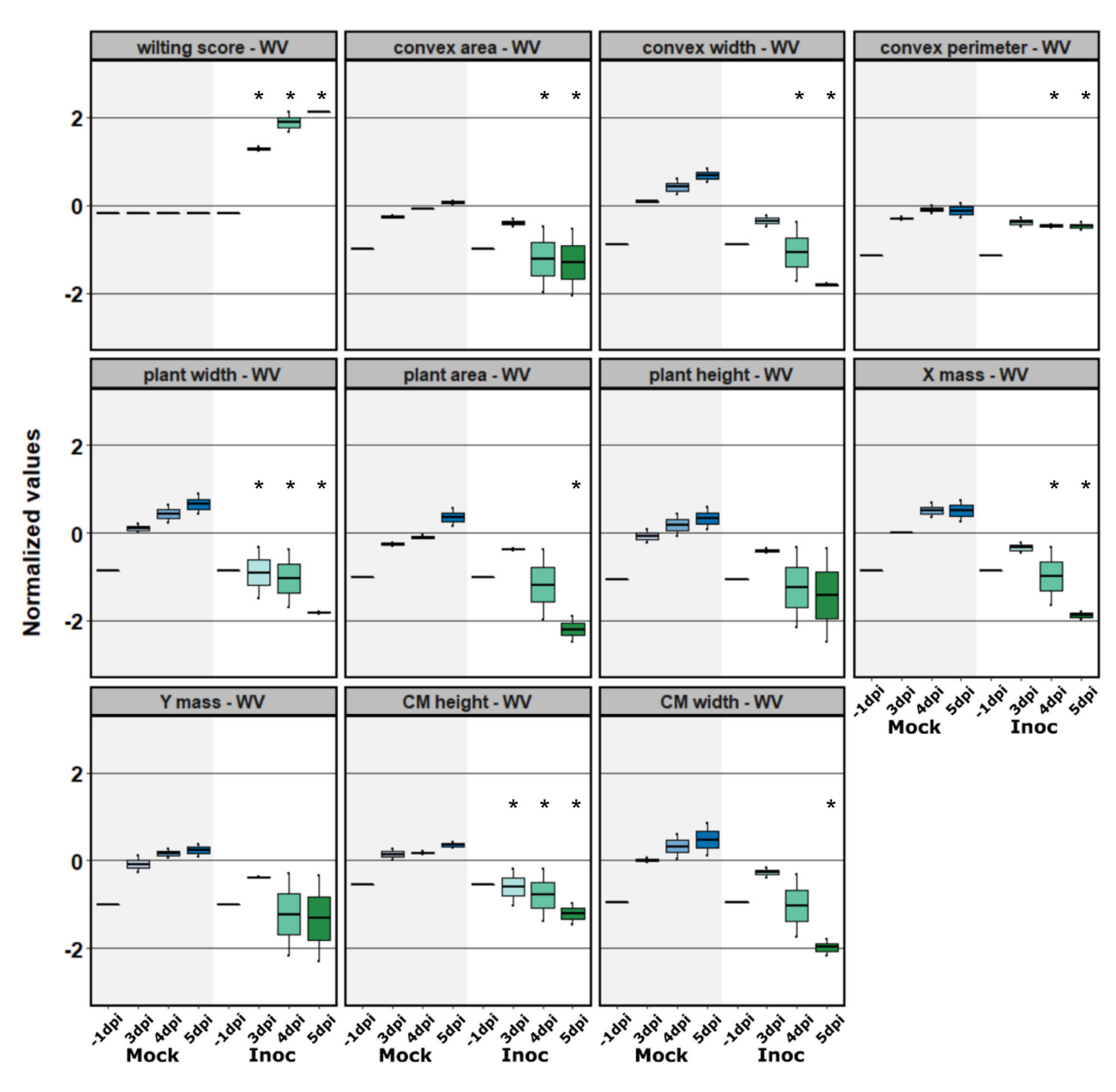


Figure 3. Trait values for descriptors in mock-treated (gray) and Ralstonia solanacearum-treated (white) susceptible parent WV from -1 to 5 dpi. Stars indicate significant differences between mock and inoculated values on the same day as determined with a one-tailed *t*-test (*P* < 0.05). dpi, days post-inoculation.

accurate towards the peak expression of a phenotype. The broad-sense heritability estimates for each image-based trait varied between 0.53 and 0.69 at 6 dpi (Figure S6; Table S3). Best linear unbiased predictor (BLUP) values calculated using a mixed linear model were used to carry out QTL mapping.

We first performed QTL analysis at each time point using the wilting scores assessed by human scoring. We also mapped the area under the disease progress curve (AUDPC) from day -1 to 8 dpi. AUDPC values provide information about disease severity over time (Simko &

Piepho, 2012). Using composite interval mapping (CIM), at a logarithm of the odd (LOD) threshold of 3, two QTLs for 'wilting score' were detected at 8 dpi on chromosomes 6 and 10; one QTL for AUDPC wilting score was detected on chromosome 10 (Table 1). The QTL on chromosome 6 was not detected at any other time point, while the region on chromosome 10 was also detected at 6 and 7 dpi. No QTLs were detected earlier than 6 dpi with visual wilting assessment.

To be consistent with previous studies of bacterial wilt QTL mapping, we call QTL 'Bacterial wilt resistance (*Bwr*)'

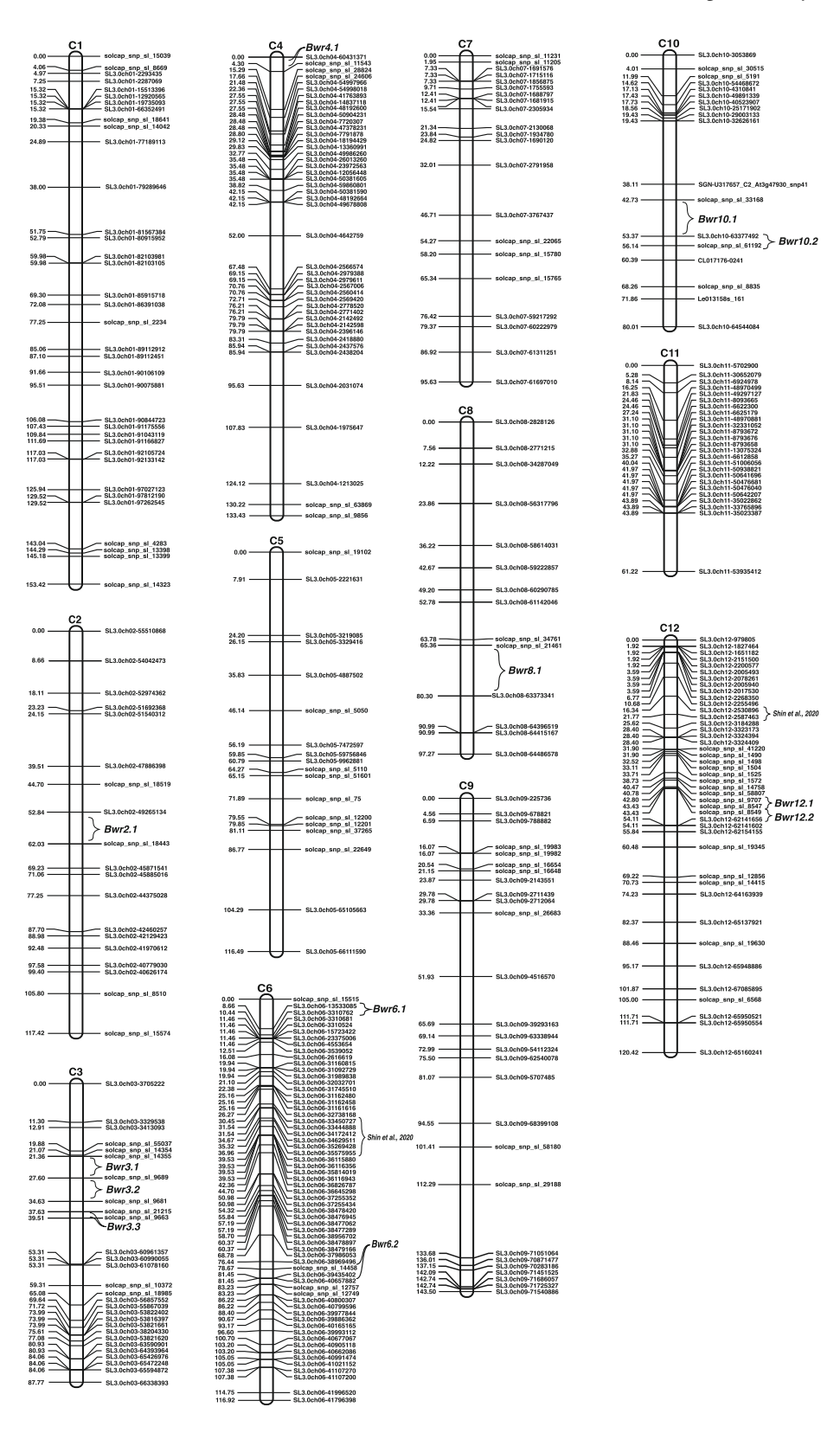


Figure 4. Genetic linkage map constructed with SolCap and genotyping by sequencing single-nucleotide polymorphism markers. Location of 12 QTL clusters displayed using left and right markers. Locations of previously identified QTLs on chromosomes 6 and 12 are also displayed (Shin et al., 2020). QTL, quantitative trait locus.

#### 894 Valérian Méline et al.

Table 1 Overview of the three QTLs identified by human visual scoring at 8 dpi and 27 QTLs identified using image-based phenotyping at 6 dpi

Chromosome	Cluster	Position	Left marker	Right marker	Trait name	LOD	PVE	Add	Left CI	Right Cl
2	Bwr2.1 62 SL3.0ch02-49265134		solcap_snp_sl_18443	CM width	3.243	5.3883	-0.25	57.5	68.5	
3	Bwr3.1	22	solcap_snp_sl_14355	solcap snp sl 9689	plant width	3.497	9.0575	0.282	21.5	25.5
3	Bwr3.1	22	solcap_snp_sl_14355	solcap_snp_sl_9689	X mass	3.468	8.5483	0.272	21.5	26.5
3	Bwr3.1	25	solcap_snp_sl_14355	solcap_snp_sl_9689	plant height	4.432	9.2885	0.322	21.5	32.5
3	Bwr3.1	25	solcap_snp_sl_14355	solcap_snp_sl_9689	Y mass	3.491	9.5048	0.295	21.5	32.5
3	Bwr3.2	29	solcap_snp_sl_9689	solcap_snp_sl_9681	AUDPC convex area	4.108	7.8596	0.317	24.5	33.5
3	Bwr3.2	30	solcap_snp_sl_9689	solcap_snp_sl_9681	AUDPC CM width	5.218	9.6273	0.361	24.5	33.5
3	Bwr3.2	30	solcap_snp_sl_9689	solcap_snp_sl_9681	AUDPC convex width	4.62	10.133	0.354	24.5	33.5
3	Bwr3.2	30	solcap_snp_sl_9689	solcap_snp_sl_9681	AUDPC plant area	4.308	7.5722	0.338	24.5	33.5
3	Bwr3.2	30	solcap_snp_sl_9689	solcap_snp_sl_9681	AUDPC plant width	4.998	10.877	0.367	24.5	33.5
3	Bwr3.2	30	solcap_snp_sl_9689	solcap_snp_sl_9681	AUDPC X mass	4.913	10.71	0.365	25.5	33.5
3	Bwr3.2	33	solcap_snp_sl_9689	solcap_snp_sl_9681	AUDPC CM height	4.817	8.994	0.338	27.5	37.5
3	Bwr3.3	38	solcap_snp_sl_21215	solcap_snp_sl_9663	CM width	5.411	9.7475	0.343	36.5	39.5
3	Bwr3.3	38	solcap_snp_sl_21215	solcap_snp_sl_9663	convex area	3.568	9.448	0.303	34.5	39.5
3	Bwr3.3	38	solcap_snp_sl_21215	solcap_snp_sl_9663	convex width	4.827	9.8091	0.329	35.5	39.5
3	Bwr3.3	38	solcap_snp_sl_21215	solcap_snp_sl_9663	plant area	3.228	8.4528	0.294	34.5	39.5
4	Bwr4.1	4	SL3.0ch04-60431371	solcap snp sl 11543	convex width	3.368	6.8646	0.277	1.5	9.5
6	Bwr6.1	10	SL3.0ch06-13533085	SL3.0ch06-3310762	AUDPC convex perimeter	4.324	7.7592	0.33	8.5	11.5
6	Bwr6.2	81	solcap_snp_sl_14458	SL3.0ch06-39435402	wilting score	3.469	11.467	-0.28	78.5	81.5
8	Bwr8.1	77	solcap_snp_sl_21461	SL3.0ch08-63373341	AUDPC convex perimeter	3.427	10.409	0.38	73.5	82.5
8	Bwr8.1	80	solcap_snp_sl_21461	SL3.0ch08-63373341	AUDPC CM width	4.947	8.3653	0.338	76.5	82.5
8	Bwr8.1	80	solcap_snp_sl_21461	SL3.0ch08-63373341	AUDPC convex area	4.018	7.2955	0.306	75.5	83.5
8	Bwr8.1	80	solcap_snp_sl_21461	SL3.0ch08-63373341	AUDPC convex width	4.37	8.6008	0.327	76.5	82.5
8	Bwr8.1	80	solcap_snp_sl_21461	SL3.0ch08-63373341	AUDPC plant width	4.346	8.4584	0.324	76.5	82.5
8	Bwr8.1	80	solcap_snp_sl_21461	SL3.0ch08-63373341	AUDPC X mass	4.291	8.3494	0.323	76.5	82.5
10	Bwr10.1	51	solcap_snp_sl_33168	SL3.0ch10-63377492	wilting score	3.342	12.197	0.355	48.5	54.5
10	Bwr10.1	53	solcap_snp_sl_33168	SL3.0ch10-63377492	AUDPC wilting score	3.382	8.6603	0.293	49.5	54.5
10	Bwr10.2	56	SL3.0ch10-63377492	solcap_snp_sl_61192	plant height	3.277	7.4686	0.289	55.5	59.5
12	Bwr12.1	43	solcap_snp_sl_9707	solcap_snp_sl_8547	Y mass	3.415	8.4996	0.281	40.5	43.5
12	Bwr12.1	51	solcap_snp_sl_8549	SL3.0ch12-62141656	CM height	4.119	11.118	0.341	44.5	54.5

Each line represents a bacterial wilt resistance QTL (*Bwr*) for a single QTL trait. Cluster: QTLs for single traits that were detected at the same left and right genetic marker. Trait name refers to the QTL trait that was detected. LOD, maximum value of the logarithm of the odd; PVE, percentage of phenotypic variance explained; Add, additive effect. A positive additive effect refers to an allele where the resistant H7996 parent had a higher trait value, and a negative sign indicates that the allele from H7996 had a lower trait value. A higher trait value is favorable for all image-based traits except for visual wilting score, where a higher trait value was associated with susceptibility (e.g., 90% wilting indicates higher susceptibility than 20% wilting). Left confidence interval (CI) and Right CI indicate the confidence interval calculated by a one-LOD decrease from the estimated QTL position. QTL, quantitative trait locus.

QTL. We use the term 'QTL cluster' to describe QTL for different traits that are detected with the same left and right genetic marker. The wilting score QTL on chromosome 6 (Table 1, *Bwr6.2*) has been detected repeatedly for resistance to other species and strains of *Ralstonia* (Figure 4;

Carmeille et al., 2006; Danesh et al., 1994; Mangin et al., 1999; Thoquet, Olivier, Sperisen, Rogowsky, Laterrot, et al., 1996; Thoquet, Olivier, Sperisen, Rogowsky, Prior, et al., 1996; Wang et al., 2000, 2013; Young & Danesh, 1994).

1365313x, 2023, 5, Downloaded from https://onlinelibrary.wiley.com/doi/10.1111/pj.16101, Wiley Online Library on [20/12/2024]. See the Terms and Conditions (https://onlinelibrary.wiley.com/terms-and-conditions) on Wiley Online Library for rules of use; OA articles are governed by the applicable Creative Commons Licensean Conditions (https://onlinelibrary.wiley.com/terms-and-conditions) on Wiley Online Library for rules of use; OA articles are governed by the applicable Creative Commons Licensean Conditions (https://onlinelibrary.wiley.com/terms-and-conditions) on Wiley Online Library for rules of use; OA articles are governed by the applicable Creative Commons Licensean Conditions (https://onlinelibrary.wiley.com/terms-and-conditions) on Wiley Online Library for rules of use; OA articles are governed by the applicable Creative Commons Licensean Conditions (https://onlinelibrary.wiley.com/terms-and-conditions) on Wiley Online Library for rules of use; OA articles are governed by the applicable Creative Commons Licensean Conditions (https://onlinelibrary.wiley.com/terms-and-conditions) on Wiley Online Library for rules of use; OA articles are governed by the applicable Creative Commons Licensean Conditions (https://onlinelibrary.wiley.com/terms-and-conditions) on Wiley Online Library for rules of use; OA articles are governed by the applicable Creative Commons (https://onlinelibrary.wiley.com/terms-and-conditions) on Wiley Online Library for rules of use of the conditions (https://onlinelibrary.wiley.com/terms-and-conditions) on Wiley Online Library for rules of use of the conditions (https://onlinelibrary.wiley.com/terms-and-conditions) on Wiley Online Library for rules of use of us

We next detected QTLs using image-based phenotyping. As plant shape at a given time point after inoculation is related to shape at day -1, the difference in value from day -1 to each time point was used for QTL mapping for each of our 10 descriptors. In addition, we mapped the AUDPC from day -1 to 6 dpi for each trait. Descriptive statistics for each trait for resistant and susceptible parents and RILs are shown in Table S4. At 6 dpi, the last time point we imaged, we identified 27 QTLs for 10 imagebased traits (Table 1; Figure 4). Each Bwr QTL explained approximately 5-12% of the variation in response to R. solanacearum. The 27 Bwr image-based QTLs were grouped into 10 clusters (Table 1; Figure 4). Anywhere between one and seven Bwr QTLs were part of a given QTL cluster, Each QTL within a cluster explained a different percentage of phenotypic variation.

All genomic regions were identified using either image-based traits or wilting score, and not both. However, on chromosome 10, wilting score and AUDPC wilting score identified Bwr10.1. Although no QTLs identified using image-based traits overlapped with Bwr10.1, plant height detected a QTL at Bwr10.2 that was in close proximity (Figure 5a).

Bwr QTLs for traits that are highly correlated with each other frequently mapped to the same loci (Figure 2b). For example, Bwr3.2 and Bwr3.3, QTLs for arearelated traits (convex width, convex area, plant area, and CM width, r > 0.84 for each comparison; Figure 2b) were detected on the proximal arm of chromosome 3 (Table 1; Figure 5b). At other loci, only one trait that described one aspect of the wilting phenotype was present. For example, despite several metrics that describe width, only convex width was identified as a QTL on chromosome 4 (Bwr4.1; LOD 3.36; phenotypic variance explained = 6.86%).

# Image-based phenotyping identified Bwr QTLs earlier than visual scoring

Although no QTLs were identified based on human scoring at any time point earlier than 6 dpi, at 3, 4, and 5 dpi, we detected image-based QTL clusters which co-localized with those identified at 6 dpi (Table S5). Bwr3.3 (plant width

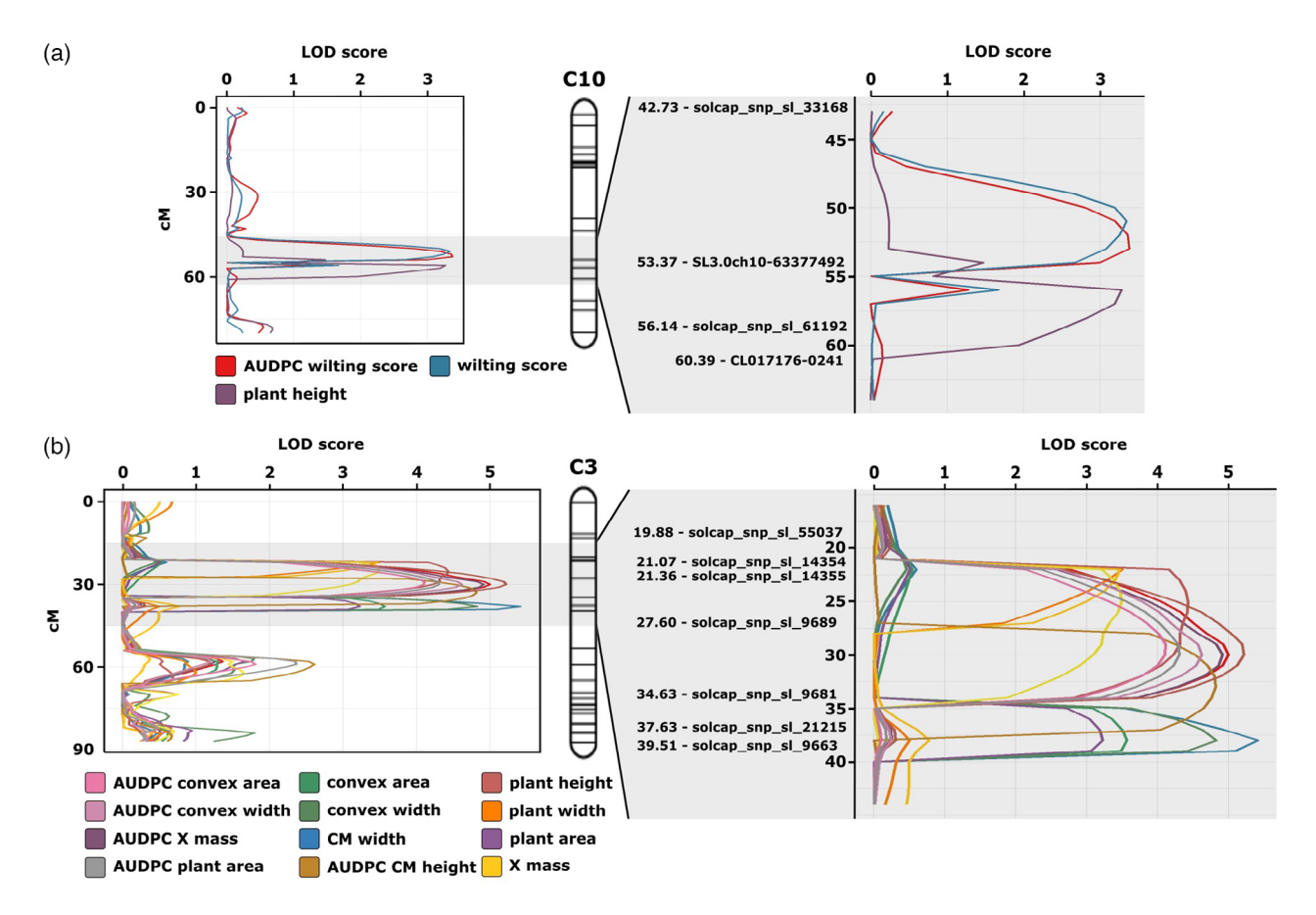


Figure 5. QTL clusters on chromosomes 10 (a) and 3 (b).

The vertical axis represents the genetic position (cM) and the horizontal axis shows the logarithm of the odd score. For each chromosome, the left panel represents the entire chromosome and the right panel represents the significant QTL cluster regions. QTL, quantitative trait locus.

#### Valérian Méline et al.

and area traits) was detected at 3, 4, 5, and 6 dpi, Bwr3.1 (plant height and width traits) was detected at 3, 5, and 6 dpi, and Bwr3.2 was detected at 3 and 6 dpi. Bwr12.1 was detected at both 5 and 6 dpi. This is consistent with the higher heritability of all image-based traits at 3 and 4 dpi compared to visual assessment (Figure S6). In this study, wilting symptoms in completely susceptible plants (such as the WV parent) begin to appear at 4 dpi, and plants are nearly 100% wilted by 6 dpi. Our results show that image-based phenotyping can identify Bwr QTLs prior to the onset of wilting symptoms.

## Multi-trait QTL analysis

Mapping for single image-based traits did not detect any QTLs at Bwr6.2, a known QTL involved in bacterial wilt resistance (Carmeille et al., 2006; Danesh et al., 1994; Mangin et al., 1999; Thoquet, Olivier, Sperisen, Rogowsky, Laterrot, et al., 1996; Thoquet, Olivier, Sperisen, Rogowsky, Prior, et al., 1996; Wang et al., 2000, 2013; Young & Danesh, 1994) which we detected with visual scoring (Figure 4: Table 1). Visual wilting score is a complex phenotype and observers capture different aspects of the plant morphology. Since the image-based traits were unidimensional, we hypothesized that individual image-based traits may not be sufficient to capture the bacterial wilt disease phenotype. To test this, we performed multi-trait QTL analysis using principal components (PCs) derived from a group of image-based traits and the visual wilting score. For these analyses, we calculated two sets of PCs. The first set of PCs included all primary image-based traits along with wilting score, and the second set of PCs included only

the image-based traits (see Tables S6 and S7 for a list of all traits used in the analysis). All days were used in both sets of PCs. QTL mapping with both sets of PCs allowed us to test whether using only image-based traits could be sufficient to detect all QTLs observed with image-based and wilting scores if they were treated as multivariate components. A total of five PCs for each set of traits were used and these captured >98% of the variation in these phenotypes as reflected in the scree plots (Table S7; Figure S7). Wilting score showed the most differential response from all the image-based phenotypes and captured >80% of the variation in PC1 and PC2 (Tables S6 and S7). Using these five PCs for each set, we detected five QTLs using PCs without wilting score and four QTLs using PC values that included wilting score. For both sets of PCs, all but one QTL were detected at or near the position of a QTL present in the single-trait analyses (Table 2). Most importantly, PC5 generated using the primary image-based traits without the wilting score detected a QTL linked to Bwr6.2 (position 81, Table 1; position 85, Table 2) which we had failed to identify using any single image-based trait. When wilting score was included in the PCs, a QTL linked to Bwr6.2 was also detected (position 79, Table 2). The detection of a QTL linked to Bwr6.2 using a multivariate summary of the image-based traits demonstrates that machine-generated phenotypes can be sufficient to model the complexity of morphological changes associated with wilting. Thus, multivariate traits expand the phenotypic space addressable by high-throughput phenotyping and disease screening and enable the identification of resistance loci that would be captured by traditional subjective scoring while also

Table 2 Multi-trait QTL analysis

Chromosome	Position	Left marker	Right marker	Trait name	LOD	PVE	Add	Left Cl	Right CI
3	30	solcap_snp_sl_9689	solcap_snp_sl_9681	PC1 without visual wilting score	4.7451	10.4055	0.3589	24.5	33.5
3	57	SL3.0ch03-61078160	solcap_snp_sl_10372	PC5 without visual wilting score	3.761	9.5337	0.3722	54.5	59.5
6	10	SL3.0ch06-13533085	SL3.0ch06-3310762	PC3 without visual wilting score	4.413	13.1285	0.3516	9.5	11.5
6	85	solcap_snp_sl_12749	SL3.0ch06-40800307	PC5 without visual wilting score	3.6518	6.0843	0.298	83.5	86.5
8	80	solcap_snp_sl_21461	SL3.0ch08-63373341	PC1 without visual wilting score	3.5015	6.8606	0.2922	75.5	82.5
3	30	solcap_snp_sl_9689	solcap_snp_sl_9681	PC1 with visual wilting score	4.6247	10.1476	0.3539	24.5	33.5
4	5	solcap_snp_sl_11543	solcap_snp_sl_28824	PC2 with visual wilting score	3.4248	9.0385	-0.3108	1.5	10.5
6	79	solcap_snp_sl_14458	SL3.0ch06-39435402	PC4 with visual wilting score	4.0312	10.745	-0.3331	76.5	80.5
8	80	solcap_snp_sl_21461	SL3.0ch08-63373341	PC1 with visual wilting score	3.4881	6.8168	0.2908	75.5	82.5

CI, confidence interval; LOD, logarithm of the odd; PVE, phenotypic variance explained; QTL, quantitative trait locus.

365313x, 2023, 5, Downloaded from https://onlinelibrary.wiely.com/doi/10.1111/tpj.16101, Wiley Online Library on [20/12/2024]. See the Terms and Conditions (https://onlinelibrary.wiely.com/terms-and-conditions) on Wiley Online Library for rules of use; OA articles are governed by the applicable Cerative Commons Licensean Conditions (https://onlinelibrary.wiely.com/terms-and-conditions) on Wiley Online Library for rules of use; OA articles are governed by the applicable Cerative Commons Licensean Conditions (https://onlinelibrary.wiely.com/terms-and-conditions) on Wiley Online Library for rules of use; OA articles are governed by the applicable Cerative Commons Licensean Conditions (https://onlinelibrary.wiely.com/terms-and-conditions) on Wiley Online Library for rules of use; OA articles are governed by the applicable Cerative Commons Licensean Conditions (https://onlinelibrary.wiely.com/terms-and-conditions) on Wiley Online Library for rules of use; OA articles are governed by the applicable Cerative Commons Licensean Conditions (https://onlinelibrary.wiely.com/terms-and-conditions) on Wiley Online Library for rules of use; OA articles are governed by the applicable Cerative Commons Licensean Conditions (https://onlinelibrary.wiely.com/terms-and-conditions) on Wiley Online Library for rules of use; OA articles are governed by the applicable Cerative Commons (https://onlinelibrary.wiely.com/terms-and-conditions) on Wiley Online Library for rules of use; OA articles are governed by the applicable Cerative Commons (https://onlinelibrary.wiely.com/terms-and-conditions) on Wiley Online Library for rules of use; OA articles are governed by the applicable Cerative Commons (https://onlinelibrary.wiely.com/terms-and-conditions) on Wiley Online Library for rules of use; OA articles are governed by the applicable Cerative Commons (https://onlinelibrary.wiely.com/terms-and-conditions) on Wiley Online Library for rules of use; OA articles are governed by the applicable Cerative Commons (https://onlinelibrary.wiely.com/term

expanding our ability to identify loci affecting individual

# Bwr QTLs occur at loci distinct from plant architecture and growth QTLs

The parents of the RIL population, H7996 and WV, have different aboveground phenotypes (Figure S4) and the shoot architecture of the RILs correspondingly varies. To determine if the Bwr QTLs were the result of tomato responses to R. solanacearum, and not due to differences in aboveground plant architecture, we used the image-based traits captured at -1 dpi, the day before plants had been inoculated, in a QTL analysis. We call these 'tomato plant architecture (Tpa)' QTLs. We identified 22 Tpa QTLs within eight QTL clusters (Table 3). Two Tpa QTLs were detected within the same interval as Bwr observed at 6 dpi: Tpa3.1 was detected near Bwr3.2 and Tpa8.1 was detected near Bwr8.1. Both Bwr3.2 and 8.1 are QTLs for AUDPC traits for plant width and area. It is possible that these two plant architecture and disease resistance QTLs co-localize due to a common genetic determinant that largely impacts plant morphology. Alternatively, two alleles where one impacts plant architecture and the other influences disease resistance are linked. None of the other Bwr QTLs co-localize with Tpa QTLs, which suggests that our image-based

disease phenotyping approach largely detected genomic regions that respond to R. solanacearum and are not the result of differential growth patterns within the RILs.

#### DISCUSSION

Breeding for disease resistance is one of the best strategies to combat plant pathogens and prevent major crop loss, but is challenging in part due to the complicated nature of disease phenotyping. Here we used non-destructive, image-based phenotyping with RGB images to identify QTLs for tomato responses to R. solanacearum, three of which were detected as early as 3 dpi. Combining our single image-based traits allowed us to detect QTLs that were only identified by visual scoring in the single-trait analysis. These results establish the importance and feasibility of quantitative, non-destructive, image-based phenotyping to identify new genetic targets for crop disease resistance breeding.

## Benefits of image-based phenotyping

Image-based phenotyping has been used to detect QTLs associated with plant root (Topp et al., 2013) and shoot (Knoch et al., 2020; Li et al., 2020; Wang et al., 2019; Zhang et al., 2017) architecture, salt stress (Awlia et al., 2021), and yield (Pauli et al., 2016; Tanger et al., 2017), among other

Table 3 Overview of tomato plant architecture (Tpa) QTLs identified at -1 dpi by image-based phenotyping

Cluster	Trait name	Chromosome	Position	Left marker	Right marker	LOD	PVE	Add	Left CI	Right Cl
Tpa2.1	convex width	2	117	solcap_snp_sl_8510	solcap_snp_sl_15574	4.2287	8.3478	0.3056	114.5	117
Tpa2.1	plant width	2	117	solcap_snp_sl_8510	solcap_snp_sl_15574	3.8821	7.5656	0.2906	114.5	117
Tpa2.1	X mass	2	117	solcap_snp_sl_8510	solcap_snp_sl_15574	4.8344	8.5043	0.312	114.5	117
Tpa3.1	plant area	3	29	solcap_snp_sl_9689	solcap_snp_sl_9681	4.0834	7.7376	0.304	25.5	34.5
Tpa3.2	convex area	3	59	SL3.0ch03-61078160	solcap_snp_sl_10372	4.412	7.5959	0.2983	57.5	62.5
Tpa3.2	X mass	3	59	SL3.0ch03-61078160	solcap_snp_sl_10372	3.4878	6.4254	0.2705	57.5	62.5
Tpa5.1	convex perimeter	5	106	SL3.0ch05-65105663	SL3.0ch05-66111590	4.2495	8.047	0.3249	99.5	112.5
Tpa6.1	CM width	6	10	SL3.0ch06-13533085	SL3.0ch06-3310762	3.9209	10.0438	0.315	8.5	11.5
Tpa6.1	convex area	6	10	SL3.0ch06-13533085	SL3.0ch06-3310762	5.5064	9.1352	0.3286	8.5	11.5
Tpa6.1	convex perimeter	6	10	SL3.0ch06-13533085	SL3.0ch06-3310762	6.0019	10.9029	0.3794	8.5	11.5
Tpa6.1	convex width	6	10	SL3.0ch06-13533085	SL3.0ch06-3310762	3.2702	6.4948	0.2701	8.5	11.5
Tpa6.1	plant area	6	10	SL3.0ch06-13533085	SL3.0ch06-3310762	4.4188	8.2091	0.3149	8.5	11.5
Tpa6.1	plant height	6	10	SL3.0ch06-13533085	SL3.0ch06-3310762	3.4395	7.7884	0.2853	8.5	11.5
Tpa6.1	plant width	6	10	SL3.0ch06-13533085	SL3.0ch06-3310762	3.7961	7.5494	0.2909	8.5	11.5
Tpa6.1	X mass	6	10	SL3.0ch06-13533085	SL3.0ch06-3310762	5.305	9.4216	0.3291	8.5	11.5
Tpa6.1	Y mass	6	10	SL3.0ch06-13533085	SL3.0ch06-3310762	4.6841	8.2847	0.3465	8.5	11.5
Tpa8.1	convex area	8	77	solcap_snp_sl_21461	SL3.0ch08-63373341	3.3939	9.0659	0.3257	73.5	82.5
Tpa8.1	convex width	8	79	solcap_snp_sl_21461	SL3.0ch08-63373341	3.3521	8.0965	0.3004	74.5	82.5
Tpa8.1	plant width	8	79	solcap_snp_sl_21461	SL3.0ch08-63373341	3.1855	7.5993	0.2908	74.5	82.5
Tpa8.1	X mass	8	80	solcap_snp_sl_21461	SL3.0ch08-63373341	3.6138	6.3813	0.27	74.5	82.5
Tpa9.1	convex area	9	67	SL3.0ch09-39293163	SL3.0ch09-63338944	3.7141	6.2079	-0.2705	60.5	69.5
Tpa10.1	convex perimeter	10	70	solcap_snp_sl_8835	Le013158s_161	3.3353	5.9224	0.2791	68.5	73.5

CI, confidence interval; LOD, logarithm of the odd; PVE, phenotypic variance explained; QTL, quantitative trait locus.

The Plant Journal published by Society for Experimental Biology and John Wiley & Sons Ltd., The Plant Journal, (2023), 113, 887-903

traits. Although image-based phenotyping has become increasingly common to quantify plant disease symptoms (Elliott et al., 2022; Lowe et al., 2017; Mahlein, 2016; Mahlein et al., 2017, 2019; Mir et al., 2019; Mochida et al., 2019; Pérez-Bueno et al., 2019; Pineda et al., 2021; Shakoor et al., 2017; Simko et al., 2017), few studies have used this technology to identify new genetic loci for plant disease resistance (Barbacci et al., 2020; Corwin et al., 2016; Fordyce et al., 2018; Yates et al., 2019). One reason for this may be that many plant disease symptoms occur at or below the leaf scale, such as spots and specks, presenting a challenge to sensor resolution to analyze them nondestructively at high throughput. For example, automated digital phenotyping of Septoria tritici Blotch on wheat (Triticum aestivum) leaves identified novel QTLs for resistance, but phenotyping was destructive and required significant manual labor to harvest, mount, and scan leaves (Yates et al., 2019). While wilting does occur at the leaf scale, we demonstrate here that it is possible to assess it at the whole plant scale. Imaging sensors are often expensive, making it more challenging to phenotype the large number of plants needed in QTL or GWA studies. Our method is low-cost and requires little manual labor other than placing the plant on the turntable and initiating imaging via a computer. Theoretically, plants can be imaged for as long as the researchers wishes. Here, we chose to image plants only until 6 dpi because after that point, the resistant plants grew so large that they grew out of the optical view of the camera (susceptible plants remained well within view for the entire experiment). Imaging longer would require a modified imaging setup and updated downstream analyses. Since we observed 100% wilting in our susceptible parent by 6 dpi, this platform was sufficient for our imaging needs. However, we continued with visual scoring until 8 dpi. At 7 and 8 dpi, no new plants initiate wilting symptoms. Instead, wilting on already symptomatic plants becomes more obvious at these time points, improving visually assessed phenotyping and QTL detection.

#### New QTLs for responses to Ralstonia in tomato

Resistance to *Ralstonia* species in solanaceous crops is quantitative (Carmeille et al., 2006; Danesh et al., 1994; Mangin et al., 1999; Thoquet, Olivier, Sperisen, Rogowsky, Laterrot, et al., 1996; Thoquet, Olivier, Sperisen, Rogowsky, Prior, et al., 1996; Wang et al., 2000, 2013; Young & Danesh, 1994). Breeding for resistance QTLs is thus the primary way forward to developing *Ralstonia*-resistant crops in the Solanaceae family. This has not been easy, in part because of the diversity of the RSSC (Prior et al., 2016; Remenant et al., 2012; Safni et al., 2014). Each species has multiple strains with overlapping, but distinct, sets of virulence proteins that promote disease (Landry et al., 2020). Varieties with effective resistance will likely have QTLs that

are effective against specific strains (strain-specific QTLs) as well as those effective against multiple strains (broad-spectrum QTLs).

Most previously identified QTLs provide resistance to R. pseudosolanacearum, and none of the previous studies used the R. solanacearum strain used in this work (Carmeille et al., 2006; Danesh et al., 1994; Mangin et al., 1999; Shin et al., 2020; Thoquet, Olivier, Sperisen, Rogowsky, Laterrot, et al., 1996; Thoquet, Olivier, Sperisen, Rogowsky, Prior, et al., 1996; Wang et al., 2000, 2013). Using visual assessment of wilting and the same RIL population of tomato (H7996 x WV) used here, one broad-spectrum QTL for resistance to multiple strains of R. pseudosolanacearum and one strain of R. solanacearum (JT-516) were previously identified on chromosome 6 (Carmeille et al., 2006; Danesh et al., 1994; Mangin et al., 1999; Shin et al., 2020; Thoquet, Olivier, Sperisen, Rogowsky, Laterrot et al., 1996; Thoquet, Olivier, Sperisen, Rogowsky, Prior, et al., 1996; Wang et al., 2000, 2013). We also identified a QTL on chromosome 6. In our study. Bwr6.2 confers approximately 11.5% of the variation, compared to 11.5-33% for Bwr6a-Bwr6d (Shin et al., 2020; Wang et al., 2013).

Previous studies also identified a major QTL on chromosome 12 that is effective for resistance against other species and strains of *Ralstonia* that explained between 15.9 and 53.9% of the variation (Shin et al., 2020). We found two clusters of QTLs on chromosome 12 for image-based traits that do not overlap with the previously detected QTLs. Within the region spanning *Bwr12.1* on chromosome 12 are one nucleotide binding site–leucine-rich repeat (NBS-LRR) disease resistance gene and a cluster of kinase-encoding genes. QTLs detected on chromosomes 2, 3, 4, 5, 8, and 10 have not been detected against other *Ralstonia* species and strains, and thus may be specific to *R. solanacearum*.

Together, our results establish the value of imagebased, non-destructive disease phenotyping for uncovering novel genetic components and new targets for quantitative disease resistance in crops. This type of phenotyping may enable the identification of broad-spectrum and durable resistance.

#### **METHODS**

## Plant growth

Seeds of 188 RILs from a cross between H7996 and WV were obtained in the F8 generation from the Asian Vegetable Research and Development Center (AVRDC) in June 2014. Seeds were propagated to the F9 generation in the field and greenhouse in West Lafayette, IN in 2014 and 2015 and were used for QTL mapping in 2019.

Seeds were sown into individually labeled 1801 traditional inserts (cell dimensions 3 1/8"  $\times$  3 1/8"  $\times$  2 1/4") and placed into 1020 flats (Hummert International, Earth City, MO, USA). One seed

per RIL per cell, along with parental controls, was grown in the same growth chamber in the Lilly Greenhouses and Growth Facility at Purdue University. Five independent experimental replicates were evaluated. Experimental replicates were conducted consecutively such that the next replicate was planted immediately after the prior replicate ended. The position of each line was completely randomized within each experimental replicate, and travs were rotated in the growth chamber throughout each experiment. The growth chamber temperature was set to 28°C, with a relative humidity of 65% and a lighting cycle of 16 h light/8 h dark. Seedlings started to emerge at 4 days after planting. Plants were inoculated with R. solanacearum at 17 days after planting when three true leaves were present. Each plant was imaged the day before inoculation (-1) and at 3, 4, 5, and 6 dpi. Plants were not imaged after 6 dpi because resistant individuals grew out of the image frame. Plants were visually assessed for wilting daily from 1 to 8 dpi. Of the total 188 RILs, 166 RILs were used for downstream analyses. In total, 19 RILs were excluded due to high variability in visual wilting score (for example, rated as 100% wilting in two replicates but 0% wilting in three replicates). RILs with standard deviation in wilting scores across five replicates that were in the top 10% of all standard deviations for the population were removed.

#### Ralstonia solanacearum growth and plant inoculation

Culturing of R. solanacearum and inoculation has been described previously (Caldwell et al., 2017). Briefly, R. solanacearum (containing a GFP reporter) was grown on casamino acid-peptoneglucose agar containing tetrazolium chloride in the dark for 48 h at 28°C. Bacteria were resuspended in sterile water to a concentration of approximately  $2 \times 10^8$  colony forming units ml<sup>-1</sup> for each experiment. For each experiment, the concentration of inoculum was confirmed through dilution plating. Pots of three-leaf plants were lightly compressed to induce wounding similar to transplant handling in field conditions. Next, 60 ml of inoculum was applied to the surrounding soil using a serological pipet.

# Visual assessment of bacterial wilt disease

Wilting scores were recorded based on visual assessment of plants daily from 1 to 8 dpi. Wilt scores were calculated by dividing the number of true leaves that were wilted by the total number of true leaves on the plant. Wilting percentage varied from 0 to 100%, with 0% being no wilting and 100% being complete wilting including the topmost portion of the stem. Plants were given a wilting percentage of 95% if the plant had all of its leaves wilted, excluding the topmost leaf. No wilting was observed for any plant at 1 or 2 dpi and these values were not used for mapping.

## Plant imaging

Plants were imaged using a Linco Linstor 2000-watt photo studio as the backdrop and Flora X fluorescent lighting, which created a small photo studio. The photo studio contained the following items: three Linco#3452 Flora X Auto Pop-Up Softbox Set 20" sets, three Linco#5140 Flora X Fluorescent 4-Socket Light Banks, three 8806 Zenith 77" Light Weight Light Stands, 12 Linco PP171050-1 photography studio E26 soft white bulbs (each 6400 K and 40 watts), one Linco#4225KB Linco Zenith Boom Arm Reflector Holder Kit, one 2020-6 Photography Studio Exclusive Premium Carrying Bag for Lighting Kit, one 4152 Linco Zenith Backdrop Stand Support System, a GEN0510T Photography Studio Green Screen Backdrop Muslin Background, a WH0510T Photography Studio White Screen Backdrop Muslin Background, and a BLK0510T Photography Studio Black Screen Backdrop Muslin Background.

Individual plants were placed on a PhotoCapture 360 turntable (Ortery Technologies) that was programmed to capture eight images around the plant (every 45°). The images were captured using an EOS 6D DSLR Canon camera with an EF 50 mm f/1.4 USM lens with 100 ISO, 11 Aperture, and 1/30 shutter speed on a stationary tripod. All camera settings were kept the same throughout all experiments. An imaging carriage was created with a square Petri dish and a fiducial marker attached to each side (Figure S1). A total of five independent replicates for each RIL and the parental controls were imaged.

# Phenotyping pipeline and image analysis

From the plant images, 10 traits were acquired for QTL analysis. A detailed description of the acquisition process was given previously (Yang et al., 2020, 2021). All traits were extracted based on plant size and shape. To eliminate any color discrepancy between images, images were automatically color-corrected using a fiducial marker consisting of a colored checkerboard with known physical dimensions and colors.

After color correction, plant pixels were segmented from the rest of the image by thresholding channels in the L\*A\*B\* color space. The thresholds used were the same as described in Yang et al. (2021). The resulting segmentation mask was improved with image morphological operations to fill holes and remove noise generated by the thresholding. The stem of the plant was identified using two neural networks, Mask R-CNN and U-Net. By locating the stem of the plant, metrics were defined that reflect the morphology of the plant. To train the neural networks, stem segmentation ground truth data were generated using Adobe Photoshop and LabelMe (a Python-based annotation tool) to mark the location of the image pixels belonging to the stem of the plant. More detail about this procedure is provided in (Yang et al., 2020,

The plant and stem masks were used in the subsequent size and shape analysis, which acquired 10 traits: total area of the plant mask (plant area), height of the plant mask (plant height), maximum width of the plant mask (plant width), perimeter of the convex hull (convex perimeter), area of the convex hull (convex area), width of the convex hull (convex width), horizontal distance between the CM of the left and right sides of the plant stem (CM width), height of the CM (CM height), x-axis distribution of the CM (X mass), and y-axis distribution of the CM (Y mass).

The plant area, plant height, and plant width were calculated from the plant mask. To calculate image-based plant height, the upper 5% of the plant material was not included, which helped eliminate the impact of immature leaves growing at the top. Using functions available in OpenCV Python Library, a convex hull was fit around the plant mask and the convex area and convex width were calculated. The convex hull was defined as the smallest convex polygon that contains all points in the image. Convex hull area described the area within the hull; convex perimeter referred to the perimeter of the entire hull. The width of the convex hull referred to the longest Euclidian distance between two points in the image. To calculate traits involving the CM, the plant mask was split into left and right halves using the stem mask (Yang et al., 2020) and the CM located for each half. The x-axis distance between CMs (CM width) and the average height of the CMs (CM height) were used as traits. Illustrations of each trait using images of the resistant parent H7996 and the susceptible parent WV are shown in Figure S4.

#### 900 Valérian Méline et al.

The extension of just one leaf can have a major impact on measured plant width, generating a disproportionately larger value. Capturing the plant material distribution inside the plant mask can overcome this issue. Using the split plant mask, the horizontal and vertical distribution of plant material was estimated. The distances at which 90% of the plant material was captured in the horizontal and vertical directions were used as the traits 'X mass distribution' and 'Y mass distribution'. The average of the same trait from all eight views around the plant was used to represent a single trait value. The units of these image-based traits are in pixels. In addition, AUDPC was calculated using the audpc function implemented in the R package *epifitter* (Madden et al., 2007). The average trait values for all the measured traits across all five replications are provided (Table S8).

#### DNA extraction, marker generation, and GBS

 $F_9$  generation RIL seeds and parental controls were grown in the greenhouse in 2-gallon pots with Metro Mix 510 soil. Tissue was collected for DNA extraction from 6-week-old plants. Leaf disc samples were collected from each RIL plant using a biopsy punch and were sent to LGC, Biosearch Technologies (Middlesex, UK). Genomic DNA was extracted and genotyped for 128 SNPs from the Tomato SolCAP panel using LGC's KASP assay. In total, 112 SNPs were obtained from each RIL using this method.

For GBS, genomic DNA was extracted from 188 F<sub>9</sub> individuals of the RIL population and from parental plants using TRIzol. Extracted DNA was treated with RNase and cleaned with phenol chloroform extraction. Sequencing libraries were prepared as described by (Elshire et al., 2011). Briefly, DNA was digested with *Pst*I and 150-bp paired end (PE) sequencing was performed on two lanes of an Illumina Hi-seq 2500 platform at the Purdue Genomics Facility.

Reads were mapped to the *S. lycopersicum* 3.0 genome using the methods of Manching et al. (2017). In brief, reads were de-multiplexed and adapter sequences were removed. Reads were filtered based on the presence of a GBS barcode on the forward read (R1), which accounts for 95.4% of the PE reads (Table S9). For these R1, 97.3% had a paired R2 read, and 2.7% did not form a pair (Table S9). R1 read pairs and R1 single reads were combined and assessed independent of pairing and treated as single-end reads for the remaining analyses (924 500 737 reads; Table S9).

Reads with a GBS barcode (95.4% of the PE reads) were subsequently filtered to remove those with an internal restriction site, lacking the expected restriction site overhang sequence at the end, or below a minimum length. After filtering, 93.0% of the reads were retained (Table S9). There was a minimum of 17 561 reads, a maximum of 16 127 292 reads, and an average of 4 480 149 reads per sample (Figure S8). Reads were mapped using BWA-MEM for PE reads, and the GATK haplotype caller was used to generate a genomic Variant Call Format (gVCF) file for downstream analysis.

In total, 74 082 SNPs were called between the population and the *S. lycopersicum* 3.0 reference genome. Many of these were SNPs between the reference genome and the population and did not vary in the population used here. Filtering for the presence of two alleles within the RIL population resulted in 2738 SNPs. Of these, the parental alleles were identified in both parents for 278 SNPs and in one parent for 698 SNPs. The remaining 1762 SNPs could not be assigned a parental origin and were not used for further analysis. The 976 SNPs with parental origin identified were filtered for a minor allele frequency greater than 0.02 and less than 0.99, which resulted in 632 high-quality SNPs.

Tomato SolCap markers and SNPs identified through GBS were used for map creation. High-quality SNPs identified from

GBS were combined with previously defined SolCap markers from LGC Biosearch Technologies for a total of 748 markers. Of the 748 markers, RlLs were represented by an average of 366 markers. The genotype density ranged from a minimum of 115 markers to a maximum of 555 markers (Figure S9). There was some residual heterozygosity in the RlLs (Figure S9b), and two RlLs with ≥10% heterozygosity were excluded from further analysis.

#### Linkage map construction

The software QTL lciMapping (Meng et al., 2015) (version 4.1) was used for map construction with all 748 markers. Redundant markers were filtered by taxon coverage using a missing rate of less than 15% and a distortion threshold at 0.001 to obtain a total of 408 unique markers. These 408 markers without anchor information were assigned to 12 linkage groups based on an LOD ('logarithm of the odds') score threshold value of 3. After grouping, the markers were ordered using the nearest neighbor algorithm (nnTwoOpt) using the rippling criterion SARF (Sum of Adjacent Recombination Frequencies) with a window size of five markers. After ordering, some markers at the end of the chromosomes were deleted when they were adding an insignificant genetic distance to the chromosome. These markers were identified after splitting the current chromosome in two subchromosomes between the longest marker interval. If the shortest sub-chromosome contained more than 20% of the markers before splitting, the two sub-chromosome were re-assembled. Otherwise, the shortest sub-chromosome was deleted.

#### **BLUP** calculations and QTL detection

Plant shape at a given time point after inoculation depends on plant shape prior to inoculation. Thus, for mapping, raw phenotypic data were considered as the difference in trait value between a given time point and day -1. Linear regression of the raw phenotypic data determined RIL accession and replication to be significant (P < 0.01) terms across all phenotypes. To control for the replication effect on phenotypes, we built a linear mixed model using RIL and replication as random effects using the *Imer* function implemented in the R package *Ime4* (Bates et al., 2015). This model was used to calculate the BLUP values for each trait across all accessions. We used the genetic variance estimates from the mixed model to calculate the broad-sense heritability on a line mean basis for each trait (Holland et al., 2003). The BLUP values were used to perform QTL mapping.

To ensure a normal distribution, the function 'orderNorm' was used to perform an ordered quantile normalization (Peterson & Cavanaugh, 2020) before QTL analysis using the package 'bestNormalize' version 1.6.1 with R software version 3.6.1 (R Core Team, n.d.). QTLs were detected using inclusive composite interval mapping with additive effects (ICIM-ADD) in IciMapping (Meng et al., 2015) (version 4.1) using a genetic mapping with a scanning step of 1 cM and a probability in stepwise regression of 0.001. The LOD significance threshold to declare a QTL significant was determined using a Type I error of 0.05 calculated using 1000 permutations (Churchill & Doerge, 1994).

## **AUTHOR CONTRIBUTIONS**

ASI-P and EJD designed the research; VM, DLC, and B-SK performed research; VM, EES, SB, CY, ASI-P, RSK, BD, and EJD analyzed data; SB, CY, and EJD contributed new computational tools; ASI-P and VM wrote the manuscript; all authors edited and approved the manuscript.

#### **ACKNOWLEDGMENTS**

We thank Chloe Caldwell for assistance with imaging, and Kristina Gans and Randy Wisser for help with GBS. This work was funded by a Purdue Seed Grant to AIP and ED, a Foundation for Food and Agriculture Research New Innovator Award to AIP, a USDA NIFA Postdoctoral Fellowship award (no. 2022-67012-36601) to RSK, an NSF award (1755401) to BPD, and the endowment of the Charles William Harrison Distinguished Professorship at Purdue University to FJD.

#### **CONFLICT OF INTEREST**

Authors declare no conflict of interest.

#### **DATA AVAILABILITY STATEMENT**

Raw images of RILs and parents for each replicate and each time point as well as genotype data are available at https://skvnet.ecn.purdue.edu/~sbairedd/downloads/Rs\_ril data/. Code is available from Dr. Edward Delp.

#### SUPPORTING INFORMATION

Additional Supporting Information may be found in the online version of this article.

- Figure S1. Design of our low-cost phenotyping platform including automatic turntable, backdrop, lightning, and RGB camera.
- Figure S2. Raw RGB pictures showing the evolution of wilting symptoms on RIL #646 at -1, 3, 4, 5, and 6 dpi. Visually assessed wilting scores are expressed in percentage of wilted leaves.
- Figure S3. Wilting of recombinant inbred lines (RILs). Boxplots show the normalized wilting scores at 8 dpi for the 166 RILs, the resistant Hawaii 7996 genotype (HA), and the susceptible West Virginia genotype (WV).
- **Figure S4.** RGB pictures showing the evolution of the traits at -1, 3, 4, 5, and 6 dpi for (a) Hawaii 7996 and (b) West Virginia. pw, plant width; ph, plant height; CMh, center of mass height; CMw, center of mass width; xm, horizontal mass distribution; ym, vertical mass distribution. The Hawaii 7996 plant shown here is the same plant used for Figure 1.
- Figure S5. Trait values differ between mock and inoculated resistant and mock and inoculated susceptible plants. (a-d) Resistant RILs 649, 657, 659, and 663. (e-h) Susceptible RILs 705, 776, 791, and 797. (i) Resistant parent Hawaii 7996 (HA). The susceptible parent West Virginia (WV) is shown in Figure 3 of the main text. For each trait, the gray column indicates mock-inoculated; the white column indicates Ralstonia-inoculated. Stars indicate significant differences between mock and inoculated plants on the same day (P < 0.05, one-tailed t-test).
- Figure S6. Broad-sense heritability (H2) estimates of 10 imagebased traits and wilting scores across all time points. Heritability estimates of image-based and visual scoring measurements.
- Figure S7. A total of five principal components captured a majority (>98%) of the variation in phenotypes as reflected in scree plots. (a) All primary image-based traits including wilting score. (b) All image-based traits without wilting score.
- Figure S8. GBS read distribution by sample (includes parental ref-
- Figure S9. (a) RIL and parental coverage and SNP density from GBS analysis. (b) Percent heterozygosity and SNP density.
- Table S1. Correlations between wilting at 6 dpi and image-based descriptors at 3, 4, and 5 dpi (Excel file).

- Table S2. Marker density per cM for each chromosome (Supporting Information file).
- Table S3. Heritability of each trait at each time point (Excel file).
- Table S4. Descriptive statistics for 10 image-based descriptors at 6 dpi, visually assessed wilting scores at 8 dpi, and the AUDPC for each descriptor and wilting score. Data are shown for the resistant parent Hawaii 7996, the susceptible parent West Virginia 700, and the RIL population (Supporting Information file).
- Table S5. Overview of QTLs identified across the genome at 3, 4, 5, 6, and 7 dpi with R. solanacearum. QTLs for visually assessed wilting were identified at 6 and 7 dpi; all others are image-based traits. Image-based traits identified the Bwr QTL as early as 3 dpi. LOD, maximum value of the logarithm of the odd; PVE, percentage of phenotypic variance explained. Left CI and Right CI indicate the confidence interval calculated by a one-LOD decrease from the estimated QTL position. †Bwr3.1, ††Bwr3.2, †††Bwr3.3, \*Bwr12.1, ^Bwr10.1

(Supporting Information file).

- Table S6. Partial contribution of variables for primary traits (without wilting score) for the first five principal components used for QTL mapping (Excel file).
- Table S7. Partial contributions of variables for primary traits including wilting score for the first five principal components used for QTL mapping (Excel file).
- **Table S8.** Values for all 166 RILs and each parent at -1, 3, 4, 5, and 6 dpi for all 10 image-based traits and human-assessed wilting scores. The average value for each genotype from five replicates is in pixels; wilting score is percentage of leaves wilted (Excel file)
- Table S9. Total PE reads and GBS read summary (Supporting Information file).

#### **REFERENCES**

- Awlia, M., Alshareef, N., Saber, N., Korte, A., Oakey, H., Panzarová, K. et al. (2021) Genetic mapping of the early responses to salt stress in Arabidopsis thaliana. The Plant Journal, 107, 544-563.
- Barbacci, A., Navaud, O., Mbengue, M., Barascud, M., Godiard, L., Khafif, M. et al. (2020) Rapid identification of an Arabidopsis NLR gene as a candidate conferring susceptibility to Sclerotinia sclerotiorum using timeresolved automated phenotyping. The Plant Journal, 103, 903-917.
- Bates, D.M., Machler, M., Bolker, B.M. & Walker, S.C. (2015) Fitting linear mixed-effects models using Ime4. Journal of Statistical Software, 67, 1-48.
- Bock, C., Parker, P., Cook, A.Z. & Gottwald, T. (2008) Visual rating and the use of image analysis for assessing different symptoms of citrus canker on grapefruit leaves, Plant Disease, 92, 530-541.
- Bock, C., Poole, G., Parker, P. & Gottwald, T.R. (2010) Plant disease severity estimated visually, by digital photography and image analysis, and by hyperspectral imaging. Critical Reviews in Plant Sciences, 29, 59-107.
- Caldwell, D., Kim, B.-S. & Iyer-Pascuzzi, A.S. (2017) Ralstonia solanacearum differentially colonizes roots of resistant and susceptible tomato plants. Phytopathology, 107, 528-536.
- Carmeille, A., Caranta, C., Dintinger, J., Prior, P., Luisetti, J. & Besse, P. (2006) Identification of QTLs for Ralstonia solanacearum race 3-phylotype Il resistance in tomato. Theoretical and Applied Genetics, 113, 110-121.
- Churchill, G.A. & Doerge, R.W. (1994) Empirical threshold values for quantitative trait mapping. Genetics, 138, 963-971.
- Colwell, R.N. (1956) Determining the prevalence of certain cereal crop diseases by means of aerial photography. Hilgardia, 26, 223-286.
- Corwin, J.A., Copeland, D., Feusier, J., Subedy, A., Eshbaugh, R., Palmer, C. et al. (2016) The quantitative basis of the Arabidopsis innate immune system to endemic pathogens depends on pathogen genetics. PLoS Genetics, 12, e1005789.
- Danesh, D., Aarons, S., McGill, G.E. & Young, N.D. (1994) Genetic dissection of oligogenic resistance to bacterial wilt in tomato. Molecular Plant-Microbe Interactions, 7, 464-471.

- Elliott, K., Berry, J.C., Kim, H. & Bart, R.S. (2022) A comparison of ImageJ and machine learning based image analysis methods to measure cassava bacterial blight disease severity. Plant Methods, 18, 86.
- Elphinstone, J.G., Allen, C., Prior, P. & Hayward, A.C. (2005) The current bacterial wilt situation: a global overview. In: Allen, C., Prior, P. & Hayward, A.C. (Eds.) Bacterial wilt disease and the Balstonia solanacearum species complex. St Paul, MN: American Phytopathological Society Press. pp. 9-28.
- Elshire, R.J., Glaubitz, J.C., Sun, Q., Poland, J.A., Kawamoto, K., Buckler, E.S. et al. (2011) A robust, simple genotyping-by-sequencing (GBS) approach for high diversity species. PLoS One, 6, e19379.
- Fordyce, R.F., Soltis, N.E., Caseys, C., Gwinner, R., Corwin, J.A., Atwell, S. et al. (2018) Digital imaging combined with genome-wide association mapping links loci to plant-pathogen interaction traits. Plant Physiology, **178** 1406-1422
- French, E., Kim, B.-S., Rivera-Zuluaga, K. & Iyer-Pascuzzi, A.S. (2018) Whole root transcriptomic analysis suggests a role for auxin pathways in resistance to Ralstonia solanacearum in tomato. Molecular Plant-Microbe Interactions, 31, 432-444.
- García, R.O., Kerns, J.P. & Thiessen, L. (2019) Ralstonia solanacearum species complex: a quick diagnostic guide. Plant Health Progress, 20, 7-13.
- Genin, S. (2010) Molecular traits controlling host range and adaptation to plants in Ralstonia solanacearum. The New Phytologist, 187, 920-928.
- Genin, S. & Denny, T.P. (2011) Pathogenomics of the Ralstonia solanacearum species complex. Annual Review of Phytopathology, 50, 67-89.
- Holland, J.B., Nyquist, W.E. & Cervantes-Martinez, C.T. (2003) Estimating and interpreting heritability for plant breeding. Plant Breeding Reviews,
- Ingel, B., Caldwell, D., Duong, F., Parkinson, D.Y., McCulloh, K.A., lyer-Pascuzzi, A.S. et al. (2021) Revisiting the source of wilt symptoms: X-ray microcomputed tomography provides direct evidence that Ralstonia biomass clogs xylem vessels. Phytofrontiers, 2, 41-51.
- Jackson, R.D. (1986) Remote sensing of biotic and abiotic plant stress. Annual Review of Phytopathology, 24, 265-287.
- Kim, B.-S., French, E., Caldwell, D., Harrington, E.J. & Iyer-Pascuzzi, A.S. (2016) Bacterial wilt disease: host resistance and pathogen virulence mechanisms. Physiological and Molecular Plant Pathology, 95, 37-43.
- Knoch, D., Abbadi, A., Grandke, F., Meyer, R.C., Samans, B., Werner, C.R. et al. (2020) Strong temporal dynamics of QTL action on plant growth progression revealed through high-throughput phenotyping in canola. Plant Biotechnology Journal, 18, 68-82.
- Landry, D., González-Fuente, M., Deslandes, L. & Peeters, N. (2020) The large, diverse, and robust arsenal of Ralstonia solanacearum type III effectors and their in planta functions. Molecular Plant Pathology, 21,
- Li, H., Feng, H., Guo, C., Yang, S., Huang, W., Xiong, X. et al. (2020) Highthroughput phenotyping accelerates the dissection of the dynamic genetic architecture of plant growth and yield improvement in rapeseed. Plant Biotechnology Journal, 18, 2345-2353.
- Lowe, A., Harrison, N. & French, A.P. (2017) Hyperspectral image analysis techniques for the detection and classification of the early onset of plant disease and stress. Plant Methods, 13, 80.
- Madden, L.V., Hughes, G. & van den Bosch, F. (2007) The study of plant disease epidemics. St Paul, MN: American Phytopathological Society.
- Mahlein, A.-K. (2016) Plant disease detection by imaging sensors parallels and specific demands for precision agriculture and plant phenotyping. Plant Disease, 100, 241-251.
- Mahlein, A.-K., Alisaac, E., Al Masri, A., Behmann, J., Dehne, H.-W. & Oerke, E.-C. (2019) Comparison and combination of thermal, fluorescence, and hyperspectral imaging for monitoring fusarium head blight of wheat on spikelet scale. Sensors, 19, 2281.
- Mahlein, A.-K., Kuska, M., Thomas, S., Bohnenkamp, D., Alisaac, E., Behmann, J. et al. (2017) Plant disease detection by hyperspectral imaging: from the lab to the field. Advances in Animal Biosciences, 8, 238-243.
- Manching, H., Sengupta, S., Hopper, K.R., Polson, S.W., Ji, Y. & Wisser, R.J. (2017) Phased genotyping-by-sequencing enhances analysis of genetic diversity and reveals divergent copy number variants in maize. G3 (Bethesda), 7, 2161-2170.
- Mangin, B., Thoquet, P., Olivier, J. & Grimsley, N.H. (1999) Temporal and multiple quantitative trait loci analyses of resistance to bacterial wilt in tomato permit the resolution of linked loci. Genetics, 151, 1165-1172.

- Mansfield, J., Genin, S., Magori, S., Citovsky, V., Sriariyanum, M., Ronald, P. et al. (2012) Top 10 plant pathogenic bacteria in molecular plant pathology. Molecular Plant Pathology, 13, 614-629.
- Meng, L., Li, H., Zhang, L. & Wang, J. (2015) QTL lciMapping: integrated software for genetic linkage map construction and quantitative trait locus mapping in biparental populations. Crop Journal, 3, 269-283
- Mir, R.R., Reynolds, M., Pinto, F., Khan, M.A. & Bhat, M.A. (2019) Highthroughput phenotyping for crop improvement in the genomics era. Plant Science, 282, 60-72.
- Mochida, K., Koda, S., Inoue, K., Hirayama, T., Tanaka, S., Nishii, R. et al. (2019) Computer vision-based phenotyping for improvement of plant productivity: a machine learning perspective. GigaScience, 8, giv153.
- Pauli, D., Andrade-Sanchez, P., Carmo-Silva, A.E., Gazave, E., French, A.N., Heun, J. et al. (2016) Field-based high-throughput plant phenotyping reveals the temporal patterns of quantitative trait loci associated with stress-responsive traits in cotton. G3 (Bethesda), 6, 865-879.
- Pérez-Bueno, M.L., Pineda, M. & Barón, M. (2019) Phenotyping plant responses to biotic stress by chlorophyll fluorescence imaging. Frontiers in Plant Science, 10, 1135.
- Peterson, R.A. & Cavanaugh, J.E. (2020) Ordered quantile normalization: a semiparametric transformation built for the cross-validation era. Journal of Applied Statistics, 47, 2312-2327.
- Pineda, M., Barón, M. & Pérez-Bueno, M.-L. (2021) Thermal imaging for plant stress detection and phenotyping. Remote Sensing, 13, 68.
- Planas-Marquès, M., Kressin, J.P., Kashyap, A., Panthee, D.R., Louws, F.J., Coll, N.S. et al. (2020) Four bottlenecks restrict colonization and invasion by the pathogen Ralstonia solanacearum in resistant tomato. Journal of Experimental Botany, 71, 2157-2171.
- Prior, P., Ailloud, F., Dalsing, B.L., Remenant, B., Sanchez, B. & Allen, C. (2016) Genomic and proteomic evidence supporting the division of the plant pathogen Ralstonia solanacearum into three species. BMC Genomics. 17, 90.
- R Core Team. (2021) R: A language and environment for statistical computing. Vienna, Australia: R Foundation for Statistical Computing. https:// www.R-project.org/
- Remenant, B., Babujee, L., Lajus, A., Médigue, C., Prior, P. & Allen, C. (2012) Sequencing of K60, type strain of the major plant pathogen Ralstonia solanacearum, Journal of Bacteriology, 194, 2742-2743.
- Safni, I., Cleenwerck, I., De Vos, P., Fegan, M., Sly, L. & Kappler, U. (2014) Polyphasic taxonomic revision of the Ralstonia solanacearum species complex: proposal to emend the descriptions of Ralstonia solanacearum and Ralstonia syzygii and reclassify current R. syzygii strains as Ralstonia syzygii subsp. syzygii subsp. nov., R. solanacearum phylotype IV strains as Ralstonia syzygii subsp. indonesiensis subsp. nov., banana blood disease bacterium strains as Ralstonia syzygii subsp. celebesensis subsp. nov. and R. solanacearum phylotype I and III strains as Ralstonia pseudosolanacearum sp. nov. International Journal of Systematic and Evolutionary Microbiology, 64, 3087-3103.
- Schandry, N. (2017) A practical guide to visualization and statistical analysis of R. solanacearum infection data using R. Frontiers in Plant Science, 8, 623.
- Scott, J., Wang, J. & Hanson, P. (2005) Breeding tomatoes for resistance to bacterial wilt, a global view. Proceedings of the 1st International Symposium on Tomato Diseases, 695, 161-172.
- Shakoor, N., Lee, S. & Mockler, T.C. (2017) High throughput phenotyping to accelerate crop breeding and monitoring of diseases in the field. Current Opinion in Plant Biology, 38, 184-192.
- Sharma, P., Johnson, M.A., Mazloom, R., Allen, C., Heath, L.S., Lowe-Power, T.M. et al. (2022) Meta-analysis of the Ralstonia solanacearum species complex (RSSC) based on comparative evolutionary genomics and reverse ecology. Microb Genom, 8, 000791.
- Shin, I.S., Hsu, J.-C., Huang, S.-M., Chen, J.-R., Wang, J.-F., Hanson, P. et al. (2020) Construction of a single nucleotide polymorphism marker based QTL map and validation of resistance loci to bacterial wilt caused by Ralstonia solanacearum species complex in tomato. Euphytica. 216, 54.
- Simko, I., Jimenez-Berni, J.A. & Sirault, X.R.R. (2017) Phenomic approaches and tools for phytopathologists. Phytopathology, 107, 6-17.
- Simko, I. & Piepho, H.-P. (2012) The area under the disease progress stairs: calculation, advantage, and application. Phytopathology, 102, 381-389.
- Stewart, E. & McDonald, B. (2014) Measuring quantitative virulence in the wheat pathogen Zymoseptoria tritici using high-throughput automated image analysis. Phytopathology, 104, 985-992.

- Stewart, E.L., Hagerty, C.H., Mikaberidze, A., Mundt, C.C., Zhong, Z. & McDonald, B.A. (2016) An improved method for measuring quantitative resistance to the wheat pathogen *Zymoseptoria tritici* using high-throughput automated image analysis. *Phytopathology*, **106**, 782–788.
- Tanger, P., Klassen, S., Mojica, J.P., Lovell, J.T., Moyers, B.T., Baraoidan, M. et al. (2017) Field-based high throughput phenotyping rapidly identifies genomic regions controlling yield components in rice. Scientific Reports, 7, 43220
- Thoquet, P., Olivier, J., Sperisen, C., Rogowsky, P., Laterrot, H. & Grimsley, N. (1996) Quantitative trait loci determining resistance to bacterial wilt in tomato cultivar Hawaii 7996. *Molecular Plant-Microbe Interactions*, 9, 826–836.
- Thoquet, P., Olivier, J., Sperisen, C., Rogowsky, P., Prior, P., Anais, G. et al. (1996) Polygenic resistance of tomato plants to bacterial wilt in the French West Indies. Molecular Plant-Microphe Interactions, 9, 837–842.
- Topp, C.N., Iyer-Pascuzzi, A.S., Anderson, J.T., Lee, C.R., Zurek, P.R., Symonova, O. et al. (2013) 3D phenotyping and quantitative trait locus mapping identify core regions of the rice genome controlling root architecture. Proceedings of the National Academy of Sciences of the United States of America, 110, E1695–E1704.
- Wang, J.-F., Olivier, J., Thoquet, P., Mangin, B., Sauviac, L. & Grimsley, N.H. (2000) Resistance of tomato line Hawaii7996 to Ralstonia solanacearum Pss4 in Taiwan is controlled mainly by a major strain-specific locus. Molecular Plant-Microbe Interactions. 13. 6–13.
- Wang, J.-F., Ho, F.-I., Truong, H.T.H., Hugan, S.-M., Balatero, C.H., Dittapongpitch, V. et al. (2013) Identification of major QTLs associated with

- stable resitance of tomato cultivar "Hawaii7996" to Ralstonia solana-cearum. Euphytica, 190, 241–252.
- Wang, X., Zhang, R., Song, W., Han, L., Liu, X., Sun, X. et al. (2019) Dynamic plant height QTL revealed in maize through remote sensing phenotyping using a high-throughput unmanned aerial vehicle (UAV). Scientific Reports, 9, 3458.
- Yang, C., Baireddy, S., Cai, E., Meline, V., Caldwell, D., Iyer-Pascuzzi, A.S. et al. (2021) Image-based plant wilting estimation. arXiv:2105.12926 [cs].
- Yang, C., Baireddy, S., Chen, Y., Cai, E., Caldwell, D., Méline, V. et al. (2020)
  Plant stem segmentation using fast ground truth generation. 2020 IEEE
  Southwest Symposium on Image Analysis and Interpretation (SSIAI), pp. 62–65.
- Yates, S., Mikaberidze, A., Krattinger, S.G., Abrouk, M., Hund, A., Yu, K. et al. (2019) Precision phenotyping reveals novel loci for quantitative resistance to sentoria tritici blotch. Plant Phenomics. 2019. 1–11.
- Young, N.D. & Danesh, D. (1994) Understanding bacterial wilt resistance in tomato through the use of DNA genetic-markers. In: Hayward, A.C. & Hartman, G.L. (Eds.) Bacterial wilt: the disease and its causative agent, Pseudomonas solanacearum. Wallingford, UK: CAB International, pp. 145–155.
- Yuliar, Nion, Y.A. & Toyota, K. (2015) Recent trends in control methods for bacterial wilt diseases caused by *Ralstonia solanacearum*. *Microbes and Environments*, 30, 1–11.
- Zhang, X., Huang, C., Wu, D., Qiao, F., Li, W., Duan, L. et al. (2017) High-throughput phenotyping and QTL mapping reveals the genetic architecture of maize plant growth. Plant Physiology, 173, 1554–1564.